Journal of Materials Chemistry C

ROYAL SOCIETY OF CHEMISTRY

PAPER

View Article Online
View Journal | View Issue

Cite this: J. Mater. Chem. C, 2025, 13, 19437

Controlling ambipolar OECT threshold voltage through acceptor unit engineering of conjugated polymers

Lei Shi,[bc] Huanzhou Yang,[b] Hongxiang Li,[d] Yazhuo Kuang,[bc] Mingyu Ma,[bc] Shuyan Shao,*[a] Zhiyuan Xie[bc] and Jian Liu*[bc]

Received 21st June 2025,
Accepted 18th August 2025

DOI: 10.1039/d5tc02396c

rsc.li/materials-c

Single-component ambipolar conjugated polymers are crucial in developing organic electrochemical transistors (OECTs) and complementary logic circuits, primarily because they simplify the fabrication process. However, ambipolar OECTs face significant challenges in achieving precise control over the threshold voltage (V_{Th}). This study demonstrates that V_{Th} can be effectively regulated by modifying the electron-withdrawing acceptor units in the conjugated polymer backbone. By comparing two ambipolar polymers, **PThDPP-BTz** and **PThDPP-BBTz**, we find that the stronger electron-withdrawing BBTz unit lowers the energy levels, enhances electrochemical doping efficiency, and significantly reduces V_{Th}. Specifically, the n-type V_{Th} shifts from 0.7 V to 0.02 V, and the p-type V_{Th} adjusts from −0.68 V to −0.61 V. Consequently, the inverter using ambipolar **PThDPP-BBTz** OECTs achieves a voltage gain of 93 V/V at V_{in} = 0.1 V, while the inverter based on ambipolar **PThDPP-BTz** OECTs shows an apparent voltage gain when V_{in} exceeds 0.6 V. This study clarifies the critical factors influencing the threshold voltage of OECT devices and introduces a methodology for precise V_{Th} regulation.

1. Introduction

Organic electrochemical transistors (OECTs) exploit ion-electron coupling within organic mixed ionic-electronic conductors (OMIECs) channels to facilitate efficient chemical-to-electronic transduction at ultra-low voltages[1] and with high transconductance.[2] These characteristics underpin their widespread adoption in flexible biosensors,[3] wearable devices,[4] and real-time health monitoring systems,[5] particularly in applications such as neural interfaces[6] and biomarker detection.[7] The device performance of an OECT is quantified by its transconductance (g_m), defined as $g_m = \frac{Wd}{l}\mu C^*(V_{Th} - V_{GS})$, where W, L, and d represent the channel width, length, and thickness, respectively; μ is the charge mobility; C^* is the volumetric capacitance; V_{Th} denotes the threshold voltage; and V_{GS} is the gate bias. The OMIECs materials are benchmarked by the material figure of merit μC^*, which is the product of charge carrier mobility and the volumetric capacitance.[8] Ambipolar OMIEC polymers, capable of simultaneously transporting holes and electrons under alternating gate biases, have garnered significant attention.[9] Such materials are particularly advantageous for complementary logic circuits in bioelectronics, which require performance-matched p-type and n-type components.[10] Using single-component ambipolar OMIEC materials in these circuits can drastically simplify the fabrication process.[11] Recently, advances in ambipolar material design have enabled their deployment in functional applications such as electrophysiological signal detection[12] and neuromorphic computing devices.[13]

The threshold voltage (V_{Th}), a pivotal parameter in ambipolar OECTs, is predominantly influenced by the energy levels of OMIECs channel materials and the film's responsiveness to ion permeation.[14] Precise control of V_{Th} is imperative for OECT-based chemical sensors and complementary logic circuits, as it critically determines the device noise tolerance and energy efficiency during operation.[15] Previous studies have identified multiple factors influencing V_{Th} in OECTs, including the electrochemical potential of the gate electrode,[16,17] the side-chain architecture of the conjugated polymer,[18] ion species[19] and concentration[15] in the electrolyte, and device structural design.[20] Prior research has yet to comprehensively examine how the intrinsic electronic properties of channel materials

[a] Institute of Molecular Aggregation Science, Tianjin University, Tianjin 300072, China. E-mail: shuyan_shao@tju.edu.cn
[b] State Key Laboratory of Polymer Science and Technology, Changchun Institute of Applied Chemistry, Chinese Academy of Sciences, Changchun 130022, P. R. China. E-mail: jian.liu@ciac.ac.cn
[c] School of Applied Chemistry and Engineering, University of Science and Technology of China, Hefei 230026, P. R. China
[d] College of Polymer Science and Engineering, State Key Laboratory of Polymer Materials Engineering, Sichuan University, Chengdu, Sichuan 610065, P. R. China

influence V_{Th}, particularly in the context of ambipolar OMIECs. To address this gap, we introduce a molecular engineering approach designed to precisely control V_{Th} in ambipolar OECTs. This strategy involves targeted chemical modifications of acceptor units embedded within the conjugated polymer backbone, enabling systematic exploration of the relationship between the material's energy landscape and its threshold voltage.

Donor–acceptor (D–A) copolymers are often used to achieve ambipolar charge transport, as their orbital coupling narrows the bandgap, enabling both p-type and n-type carrier injection.[10,21,22] We chose thiophene diketopyrrolopyrrole (ThDPP) as the copolymerization unit because of its electron-accepting capacity and planar backbone geometry,[23] which are widely used in designing high mobility organic electronic devices[24,25] and OMIECs.[26] To increase its solubility, we introduced ethylene glycol side chains (R) to ThDPP.[27–29] Two conjugated polymers were synthesized using benzothiadiazole (BTz) and benzobisthiadiazole (BBTz) as comonomer units. Two copolymers exhibit ambipolar charge transport characteristics. **PThDPP-BTz** displayed relatively balanced p-type and n-type characteristics. With the enhanced electron-withdrawing capability of the acceptor units, the lowest unoccupied molecular orbital (LUMO) energy levels progressively decreased. A downward shift in the energy levels of the channel material effectively reduces the charge injection barrier.[30] It facilitates electrochemical doping, lowering the V_{Th} of OECTs. This modification enabled precise V_{Th} tuning: the n-type V_{Th} shifts from 0.7 V to 0.02 V, and the p-type V_{Th} adjusts from −0.68 V to −0.61 V. A significant decrease in the n-type threshold voltage is achieved by the adjustment of the receptor unit alone, and this change is precisely related to the electronic properties of the channel material. As a result, an organic complementary inverter based on ambipolar **PThDPP-BBTz** achieves a high voltage gain of 93 V/V at V_{in} = 0.1 V. In contrast, the inverter based on ambipolar **PThDPP-BBTz** OECTs shows an apparent voltage gain only when V_{in} exceeds 0.6 V. By directly linking chemical structural changes to mixed conducting behavior, this work provides a pathway to tailor device performance through rational design of polymer energetics.

2. Results and discussions

2.1. Polymer synthesis and characterization

The conjugated polymers **PThDPP-BTz** and **PThDPP-BBTz** (Fig. 1a) were synthesized through a Pd-catalyzed Stille polymerization reaction between tributyltin-ThDPP and dibrominated benzothiadiazole (BTz) or benzobisthiadiazole (BBTz) derivatives. Purification was carried out using a Soxhlet extractor with sequential solvent extraction (methanol, hexane, acetone, and chloroform) to eliminate impurities and low-molecular-weight species. High-molecular-weight copolymers were isolated from the final hexafluoroisopropyl alcohol (HFIP) fraction. The purified polymers were subsequently dissolved in HFIP, precipitated in cold methanol, filtered, and vacuum-dried. Detailed synthetic and purification protocols are described in the SI (Fig. S1). The molecular weights and dispersity indices of the two polymers were determined by gel permeation chromatography (GPC) with polystyrene standards, using hexafluoroisopropyl alcohol (HFIP) as the eluent. The number-average molecular weight (M_n) and dispersity ($Đ$) values were estimated to be 4.9 kg mol^{-1}/2.65 for **PThDPP-BTz** and 6.4 kg mol^{-1}/4.2 for **PThDPP-BBTz** (Fig. S2). Thermal stability was evaluated through thermogravimetric analysis (TGA), where the decomposition onset temperature (T_d) was defined as the temperature at 5% weight loss. Both copolymers displayed excellent thermal stability, with T_d values of 359 °C for **PThDPP-BTz** and 303 °C for **PThDPP-BBTz** (Fig. S3).

Cyclic voltammetry (CV) measurements were conducted on thin films of **PThDPP-BTz** and **PThDPP-BBTz**. These measurements were performed against the ferrocene/ferrocenium (Fc/Fc^+) redox couple, utilizing an Ag/AgCl reference electrode to determine the electronic energy levels of the materials. The HOMO and LUMO energy levels obtained from the cyclic voltammetry measurements are −5.17 eV/−3.66 eV for

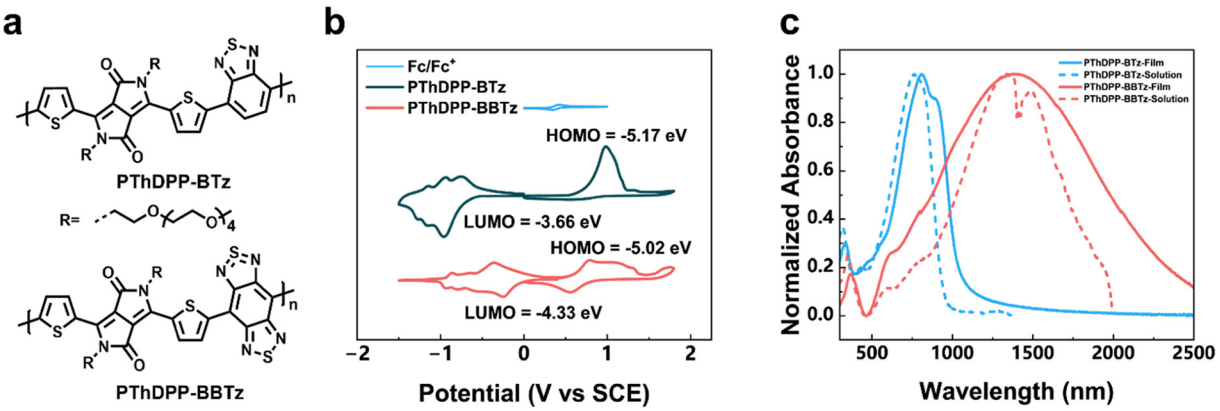

Fig. 1 (a) Chemical structures of **PThDPP-BTz** and **PThDPP-BBTz**. (b) thin-film cyclic voltammograms of **PThDPP-BTz** and **PThDPP-BBTz**. (c) Normalized UV-vis-NIR absorption spectra of **PThDPP-BTz** and **PThDPP-BBTz** in dilute HFIP (10^{-5} M) and in films (spin-coated from HFIP solutions).

Table 1 Optical properties, electrochemical properties, and energy levels of two conjugated polymers

Polymer	λ_{sol} (nm)	λ_{film} (nm)	E_{LUMO} (eV)	E_{HOMO} (eV)	E_g^{opt} (eV)	E_g^{CV} (eV)
PThDPP-BTz	761	810	−3.66	−5.17	1.36	1.51
PThDPP-BBTz	1334	1391	−4.33	−5.02	0.55	0.69

PThDPP-BTz and −5.02 eV/−4.33 eV for **PThDPP-BBTz**, respectively. The resulting plots from the first cycle are shown in Fig. 1b, and the corresponding data are summarized in Table 1. These energy level values provide insights into the electronic properties of the two conjugated polymers. Specifically, for **PThDPP-BBTz**, the deeper LUMO (lowest unoccupied molecular orbital) and shallower HOMO (highest occupied molecular orbital), as well as the corresponding narrower bandgap, originate from the stronger electron-withdrawing ability and quinone-type resonance characteristics of the BBTz unit.

Fig. 1c shows ultraviolet-visible-near-infrared (UV-vis-NIR) absorption spectroscopy for pristine **PThDPP-BTz** and **PThDPP-BBTz** in hexafluoroisopropyl alcohol and as thin films. We assigned the first peak to the π–π* transition and the second to the characteristic intramolecular charge transfer transition. In solution, the absorption maxima for **PThDPP-BTz** and **PThDPP-BBTz** were recorded at 761 nm and 1334 nm, respectively. In thin films, both **PThDPP-BTz** and **PThDPP-BBTz** exhibited red shifts in their absorption maxima, measuring 810 nm and 1391 nm, respectively. This shift is attributed to enhanced interchain π–π stacking in the solid state. Notably, the **PThDPP-BBTz** film displayed distinct redshifted absorption peaks and a broader ICT band around 1391 nm, which is linked to the increased electron-accepting ability and quinone-type resonance of the BBTz unit (Fig. S4). Both polymers demonstrate narrow bandgaps, highlighting their potential as ambipolar charge transport materials.

The spectroelectrochemical measurements were conducted to study the doping kinetics of two polymer films processed in the electrolyte (0.1 M NaCl aqueous solution). Both films exhibited decreased intensity of the characteristic bathochromic neutral absorption peak associated with ICT as the applied stepwise voltage progressively increased. Additionally, the **PThDPP-BTz** showed new absorption peaks in the long-wavelength region, irrespective of whether they underwent reduction or oxidation, which can be attributed to the formation of polarons after doping (Fig. 2). It is worth noting that the formation of the polaron absorption peak is not visible due to the redshift of the **PThDPP-BBTz** absorption peak. These results suggest that the two polymers can be readily p-doped or n-doped, promising for ambipolar charge transport.

2.2. Film microstructures

The performance of semiconducting polymers is critically dependent on their molecular packing. Grazing incidence wide-angle X-ray scattering (GIWAXS) was utilized to investigate these features (Fig. 3). The **PThDPP-BTz** film exhibits a

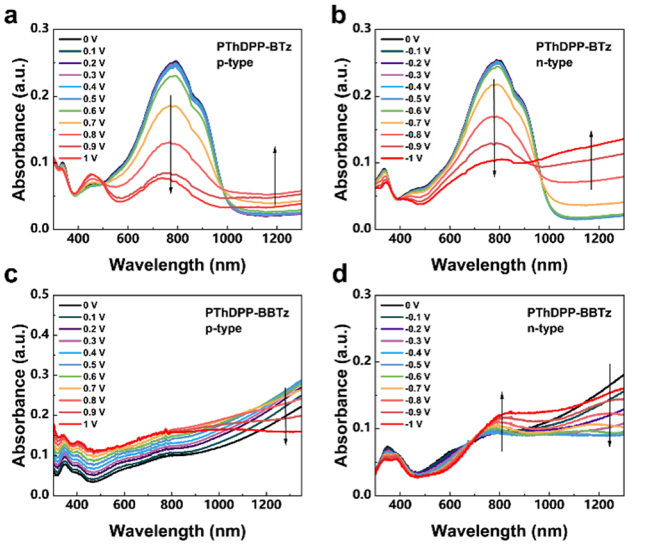

Fig. 2 Potential-dependent UV-vis-NIR absorption spectra of (a) and (b) **PThDPP-BTz** and (c) and (d) **PThDPP-BBTz** films.

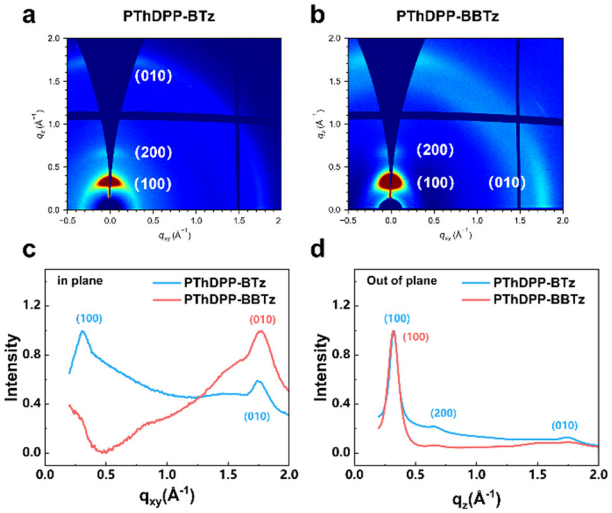

Fig. 3 Molecular packing and morphology characterization. 2D-GIWAXS pattern of (a) **PThDPP-BTz** and (b) **PThDPP-BBTz** and the corresponding (c) in-plane and (d) out-of-plane line cuts.

predominant "edge-on" molecular orientation, as evidenced by distinct scattering patterns: a strong in-plane (010) π–π stacking peak at 1.74 Å^{-1} and out-of-plane (100) and (200) diffraction signals corresponding to lamellar packing. Further analysis confirmed this edge-on alignment, with **PThDPP-BTz** showing an in-plane (010) π–π scattering peak at 1.78 Å^{-1} and an out-of-plane (100) lamellar peak at 0.32 Å^{-1}. The lamellar spacing for **PThDPP-BTz** was calculated as 2.04 nm in the out-of-plane direction, larger than that (1.96 nm) of **PThDPP-BBTz**. Similarly, the π–π stacking distances derived from the (010) peaks were 0.361 nm for **PThDPP-BTz** and 0.354 nm for **PThDPP-BBTz**, reflecting tighter intermolecular interactions in the latter. **PThDPP-BBTz** exhibit more orderly stacking

implying it is expected to be used as an excellent electronic device. To further determine the crystallinity of films, we calculated paracrystallinity (g). The results of π–π packing paracrystallinity of **PThDPP-BTz** and **PThDPP-BBTz** films are 24.9%, 25.1%, respectively.

2.3. OECT device fabrication and characterization

The performance of organic electrochemical transistors (OECTs) was characterized using a conventional planar architecture featuring interdigital electrodes (4 pairs), with channel dimensions of width (W) = 400 μm and length (L) = 30 μm. Device operation was conducted in 0.1 M NaCl aqueous electrolyte using a standard Ag/AgCl wire gate electrode (Fig. 4a). Ambipolar OMIECs demonstrated carrier-type modulation from hole-dominated to electron-dominated transport through systematic gate voltage variation.[31] Consequently, the fabricated OECTs exhibited dual operational modes, manifesting both p-type and n-type charge transport characteristics under controlled bias voltage conditions. Fig. 4b and e present the representative output characteristics of **PThDPP-BTz**- and **PThDPP-BBTz**-based OECTs, demonstrating dual p- and n-type transport properties through gate voltage modulation. Transfer characteristics for both carrier types were systematically investigated by varying V_{DS} and V_{GS} values (Fig. 4c–g). The devices achieved transconductance values of 0.4/2.4 and 3.8/8.8 S cm^{-1} for p/n-type operation of **PThDPP-BTz** and **PThDPP-BBTz**, respectively. Normalized transconductance ($g_{m,norm}$), calculated as $g_{m,norm} = g_m L/Wd$ to eliminate geometric influences, revealed balanced ambipolar performance in the **PThDPP-BBTz**-based OECTs with $g_{m,norm}$ values of 4.7 S cm^{-1} (n-type) and 3.0 S cm^{-1} (p-type), compared to 4.4 S cm^{-1} (n-type) and 0.4 S cm^{-1} (p-type) for **PThDPP-BTz** (Table 2). The weaker acceptor unit in **PThDPP-BTz** resulted in a higher n-type threshold voltage (V_{Th} = 0.7 V), while the stronger acceptor in **PThDPP-BBTz** downshifts the LUMO level (Fig. 1b), reducing V_{Th} to 0.02 V (Fig. S5). **PThDPP-BBTz** exhibited balanced μC^* values of 13.8 ± 0.9 F cm^{-1} V^{-1} (p-type) and 12.2 ± 0.8 F cm^{-1} V^{-1} (n-type), outperforming the counterpart material. The volumetric capacitance (C^*) was determined *via* electrochemical impedance spectroscopy (EIS) (Fig. S6). **PThDPP-BTz** demonstrated higher C^* values compared to **PThDPP-BBTz**, with p-type and n-type capacitances of 253 F cm^{-3} and 318 F cm^{-3}, respectively. Hole and electron mobilities (μ) were calculated as 0.07 ± 0.005/0.046 ± 0.002 cm^2 V^{-1} s^{-1} for **PThDPP-BBTz** and 0.012 ± 0.001/0.054 ± 0.002 cm^2 V^{-1} s^{-1} for **PThDPP-BTz** (Table 2). The more balanced hole/electron transport observed in **PThDPP-BBTz** may originate from the incorporation of a stronger acceptor unit BBTz, which reduces the LUMO level while elevating the HOMO level. Transient response measurements of ambipolar OECTs revealed comparable switching times for both polymers

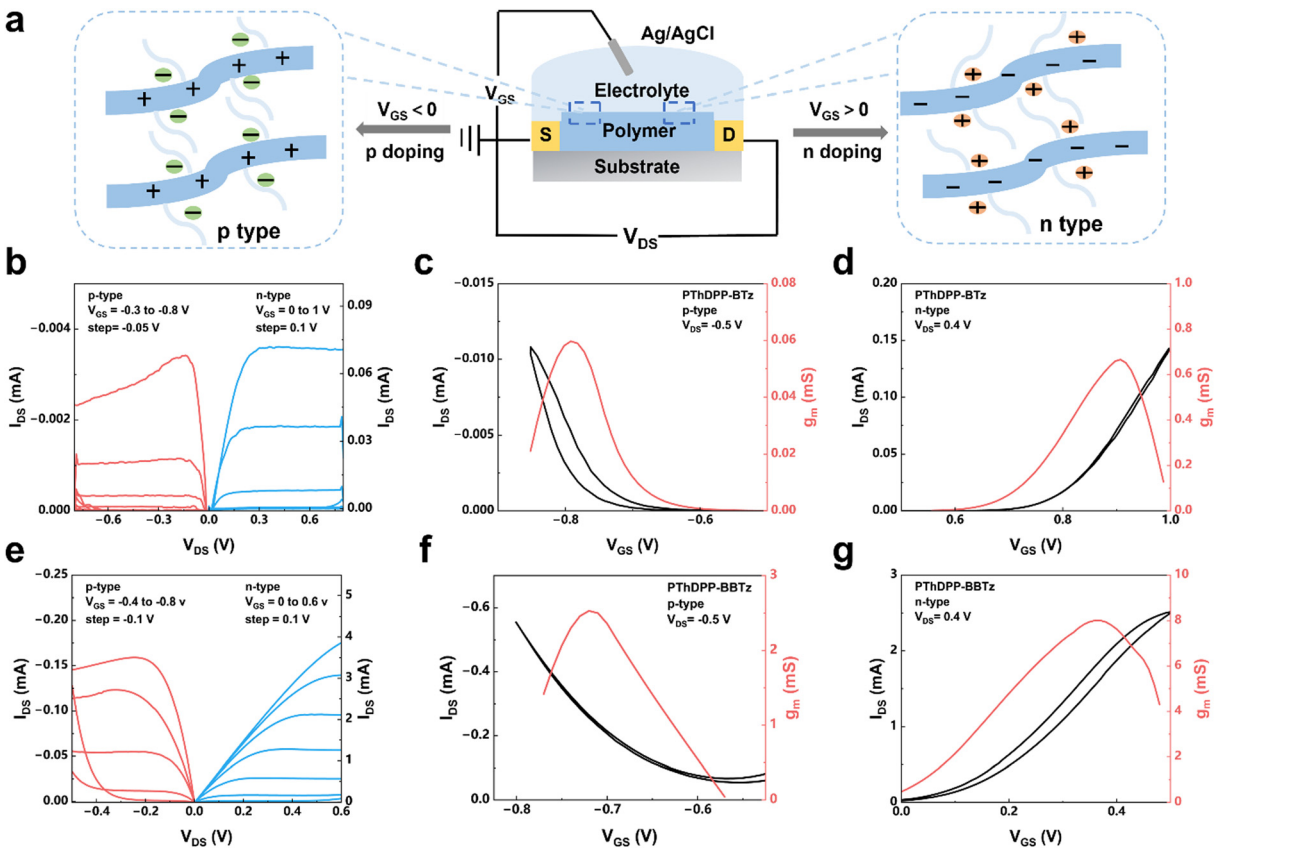

Fig. 4 (a) The device structure of ambipolar OECT. Output and Transfer characteristics of OECTs based on (b)–(d) **PThDPP-BTz** and (e)–(g) **PThDPP-BBTz**.

Table 2 OECT device performance of the two polymers

Polymer	Type	$g_{m,norm}$ (S cm^{-1})	V_{Th} (V)	μC^* (F cm^{-1} V^{-1} s^{-1})	C^* (F cm^{-3})	μ (cm^2 V^{-1} s^{-1})
PThDPP-BTz	p	0.4 ± 0.1	−0.68	3.0 ± 0.2	253.2 ± 5	0.012 ± 0.001
	n	4.4 ± 0.2	0.70	17.2 ± 0.6	318.1 ± 10	0.054 ± 0.002
PThDPP-BBTz	p	3.0 ± 0.2	−0.61	13.8 ± 0.9	172.9 ± 5	0.079 ± 0.005
	n	4.7 ± 0.2	0.02	12.2 ± 0.5	264.2 ± 5	0.046 ± 0.002

The above parameters are averaged over six devices.

(Fig. S7): **PThDPP-BTz** exhibited τ_{on}/τ_{off} = 102.6/41.1 ms (p-type) and 23.7/7.4 ms (n-type), while **PThDPP-BBTz** showed 133.2/11.1 ms (p-type) and 113.1/19.4 ms (n-type).

2.4. Application on complementary inverter

The development of efficient logic circuits demands high-performance p-type[32] and n-type[33] OECTs operating in tandem. While conventional unipolar materials necessitate complex multi-step lithography, etching, and deposition processes, ambipolar conjugated polymers—capable of dual carrier transport modulated by gate voltage—offer a streamlined pathway for circuit fabrication.[34] Here, organic complementary inverters were fabricated using **PThDPP-BTz** and **PThDPP-BBTz** ambipolar polymers as single-component channel materials (Fig. 5). These polymers exhibited distinct ambipolar transfer characteristics, with **PThDPP-BBTz** displaying a narrower bandgap than **PThDPP-BTz**. The transfer characteristics of an inverter exhibit a high output voltage (usually close to V_{DD}), a transition area, and finally a low output voltage (usually close to zero) as the V_{in} increases. The V_{out} functions as logic low before the transition area, and the corresponding V_{in} voltage functions as logic high. On the contrary, the V_{out} exhibits logic low after the transition area, and the corresponding V_{in} voltage exhibits logic high. Voltage transfer curves (VTCs) of the inverters were analyzed under varying supply voltages (V_{DD}) (Fig. 5b and c). **PThDPP-BTz**-based inverters showed a two-stage output voltage (V_{out}) transition due to their high p- and n-type threshold voltages (V_{Th}), which prevented fast p/n-OECTs switching even at V_{DD} = 1.3 V, yielding a voltage gain of 101 V V^{-1} at V_{DD} = 1.3 V and V_{in} = 0.65 V. In contrast, **PThDPP-BBTz**—with balanced hole/electron mobility and a lower threshold voltage—enabled functional inverters at V_{DD} as low as 0.4 V (Fig. 5). The switching input voltage shifted from −0.08 V to 0.1 V as V_{DD} increased from 0.4 V to 0.8 V, yielding a voltage gain of 93 V V^{-1} finally (V_{in} = 0.1 V, V_{DD} = 0.8 V). This considerably low input voltage to maintain a high gain highlights the material's potential for bioelectronic applications requiring minimal operating voltages, such as electrocardiogram (ECG)[25] or electrooculogram (EOG)[35] signal monitoring.

3. Conclusions

In this study, we demonstrate a molecular engineering strategy to precisely modulate the threshold voltage of ambipolar organic electrochemical transistors (OECTs) through the rational design of acceptor units in conjugated polymers. By synthesizing two polymers, **PThDPP-BTz** and **PThDPP-BBTz**, we systematically investigated how the electron-withdrawing

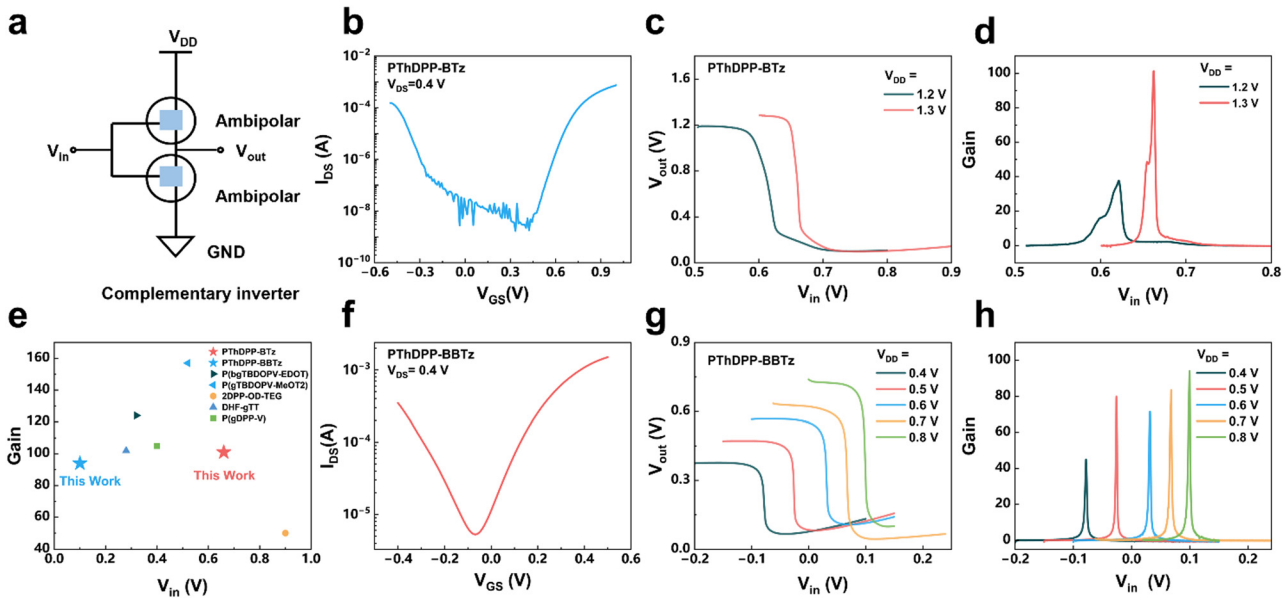

Fig. 5 (a) The complementary inverter structure. Voltage transfer characteristics and gain of the complementary inverters based on (b)–(d) **PThDPP-BTz** and (f)–(h) **PThDPP-BBTz**. (e) Summarized gain values of the inverters based on ambipolar OECTs in various V_{in}.

strength of acceptor units governs energy level alignment, electrochemical doping efficiency, and ultimately device performance. The incorporation of the stronger acceptor BBTz into **PThDPP-BBTz** significantly downshifted the LUMO level (−4.33 eV *vs.* −3.66 eV for **PThDPP-BTz**), enabling efficient electron injection and reducing the n-type V_{Th} from 0.7 V to 0.02 V while adjusting the p-type V_{Th} from −0.68 V to −0.61 V. The optimized hole/electron transport balance and low V_{Th} of the **PThDPP-BBTz**-based OECT lead to a single-component organic invertor with a high voltage gain of 93 V/V at V_{in} = 0.1 V. In contrast, the inverter based on ambipolar **PThDPP-BTz** OECTs shows an apparent voltage gain only when V_{in} exceeds 0.6 V. These results underscore the critical role of acceptor unit selection in tailoring mixed ionic-electronic conduction of conjugated polymers for OECT applications. Our work establishes a structure–property framework for designing high-performance, single-component ambipolar OMIECs, offering a pathway to simplify fabrication processes in energy-efficient bioelectronic circuits and enabling precise control over device operational parameters.

4. Experimental section/methods

4.1. Materials and characterization

The synthesis details and chemical characterization of cyclic voltammetry (CV) and gel permeation chromatography (GPC) can be found in the SI. All reagents and solvents were purchased from Innochem, Sigma-Aldrich, and Energy-Chemical, and anhydrous toluene was distilled using standard procedures.

4.2. OECT device fabrication and characterization

The glass substrates were sequentially ultrasonic cleaned with deionized water, acetone, and isopropyl alcohol. Before the experiment, the glass slides were UV-Ozone treated. For OECTs, the cleaned large-size glass slides were patterned with AZ 5214, exposed with MDA-400M aligner, and developed in NMD-3 followed by evaporation of 5 nm Cr and 40 nm Au to fabricate the source and drain electrodes. Metal liftoff was done in N-methyl pyrrolidone, followed by a rinse with acetone/isopropanol. The thin films were prepared by spin-coating the polymer solution on the substrates at 1500 rpm for 45 s. The resulting films were annealed at 150 °C for 30 min. The OECT characterization was performed by the Keysight B2902 B. The details are elaborated on in the SI. A PDMS tank was placed upon the polymer film to confine the 0.1 M NaCl (aq.), and an Ag/AgCl pellet electrode was used as the gate to perform the OECTs characterization.

4.3. Electrochemical impedance spectroscopy (EIS)

Electrochemical impedance spectroscopy was performed by Zahner Zennium XC. The details are elaborated on in the SI. Concisely, a photoresist patterned layer of Au was deposited onto the ITO, and polymer was spun-cast on the Au to serve as a working electrode (WE). 0.1 M NaCl was used as an electrolyte and constrained by a PDMS tank. Ag/AgCl and Pt wire served as the reference electrode (RE) and counter electrode (CE), respectively.

Author contributions

Lei Shi: polymer synthesis and chemical characterization. Writing – original draft. Huanzhou Yang: OECT characterization. Yazhuo Kuang: complementary inverter design. Hongxiang Li: experiment supporting. Mingyu Ma: experiment supporting. Shuyan Shao: investigation and resources. Zhiyuan Xie: supervision and resources. Jian Liu: conception, supervision and writing – review & editing.

Conflicts of interest

There are no conflicts to declare.

Data availability

The date that support the findings of this study have been included in the main text and SI. Supplementary information: Experimental methods; Fig. S1: synthetic routes to polymers; Fig. S2: GPC images; Fig. S3: TGA images; Fig. S4: absorption spectrum; Fig. S5–S8: OECT characterization; Fig. S19–S12: NMR spectra. See DOI: **https://doi.org/10.1039/d5tc02396c**

Raw data are available from the corresponding author upon reasonable request.

Acknowledgements

The authors are grateful for the financial support from the National Natural Science Foundation of China (No. 52273201, 52473199, 62105239). J. L. thanks the financial support from the Jilin Scientific and Technological Development Program (No. 20240101172JC) and a grant for Distinguished Young Scholars of the National Natural Science Foundation of China (Overseas). The project was supported by Open Research Fund of State Key Laboratory of Polymer Science and Technology, Changchun Institute of Applied Chemistry, Chinese Academy of Sciences. A portion of this work is based on the data obtained at Beijing Synchrotron Radiation Facility (BSRF) and Shanghai Synchrotron Radiation Facility (SSRF). The authors gratefully acknowledge the cooperation of the beamline scientists at BSRF-1W1A, SRRF-BL16B1 and SRRF-BL02U2.

References

1 R. Ding, X. Zhang, R. Yan, M. Peng, S. Su, S. Y. Jeong, H. Y. Woo, X. Guo, K. Feng and Z. H. Guo, *Adv. Funct. Mater.*, 2024, **35**, 2412181.
2 J. Rivnay, S. Inal, A. Salleo, R. M. Owens, M. Berggren and G. G. Malliaras, *Nat. Rev. Mater.*, 2018, **3**, 17086.

3 Z. Lu, K. Xu, K. Xiao, Q. Xu, L. Wang, P. Li, J. Zhou, D. Zhao, L. Bai, Y. Cheng and W. Huang, *npj Flexible Electron.*, 2025, **9**, 9.
4 Z. Tian, Z. Zhao and F. Yan, *Wearable Electron.*, 2024, **1**, 1–25.
5 C. Y. Go, J. Shin, M. K. Choi, I. H. Jung and K. C. Kim, *Adv. Mater.*, 2023, **36**, 2311155.
6 M. Wu, K. Yao, N. Huang, H. Li, J. Zhou, R. Shi, J. Li, X. Huang, J. Li, H. Jia, Z. Gao, T. H. Wong, D. Li, S. Hou, Y. Liu, S. Zhang, E. Song, J. Yu and X. Yu, *Adv. Sci.*, 2023, **10**, 2300504.
7 H. Liu, J. Song, Z. Zhao, S. Zhao, Z. Tian and F. Yan, *Adv. Sci.*, 2024, **11**, 2305347.
8 J. Tropp, D. Meli and J. Rivnay, *Matter*, 2023, **6**, 3132–3164.
9 Y. Lei, P. Li, Y. Zheng and T. Lei, *Mater. Chem. Front.*, 2024, **8**, 133–158.
10 A. Giovannitti, C. B. Nielsen, D.-T. Sbircea, S. Inal, M. Donahue, M. R. Niazi, D. A. Hanifi, A. Amassian, G. G. Malliaras, J. Rivnay and I. McCulloch, *Nat. Commun.*, 2016, **7**, 13066.
11 J. J. Samuel, A. Garudapalli, A. A. Mohapatra, C. Gangadharappa, S. Patil and N. P. B. Aetukuri, *Adv. Funct. Mater.*, 2021, **31**, 2102903.
12 G.-Y. Ge, J. Xu, X. Wang, W. Sun, M. Yang, Z. Mei, X.-Y. Deng, P. Li, X. Pan, J.-T. Li, X.-Q. Wang, Z. Zhang, S. Lv, X. Dai and T. Lei, *Nat. Commun.*, 2025, **16**, 396.
13 Z. Laswick, X. Wu, A. Surendran, Z. Zhou, X. Ji, G. M. Matrone, W. L. Leong and J. Rivnay, *Nat. Commun.*, 2024, **15**, 6309.
14 D. Ohayon, V. Druet and S. Inal, *Chem. Soc. Rev.*, 2023, **52**, 1001–1023.
15 P. Romele, M. Ghittorelli, Z. M. Kovács-Vajna and F. Torricelli, *Nat. Commun.*, 2019, **10**, 3044.
16 S. T. M. Tan, G. Lee, I. Denti, G. LeCroy, K. Rozylowicz, A. Marks, S. Griggs, I. McCulloch, A. Giovannitti and A. Salleo, *Adv. Mater.*, 2022, **34**, 2202359.
17 S. E. Doris, A. Pierre and R. A. Street, *Adv. Mater.*, 2018, **30**, 1706757.
18 P. Schmode, A. Savva, R. Kahl, D. Ohayon, F. Meichsner, O. Dolynchuk, T. Thurn-Albrecht, S. Inal and M. Thelakkat, *ACS Appl. Mater. Interfaces*, 2020, **12**, 13029–13039.
19 D. Ohayon, A. Hamidi-Sakr, J. Surgailis, S. Wustoni, B. Dereli, N. Wehbe, S. Nastase, X. Chen, I. McCulloch, L. Cavallo and S. Inal, *J. Am. Chem. Soc.*, 2025, **147**, 12523–12533.
20 J. Rivnay, P. Leleux, M. Sessolo, D. Khodagholy, T. Hervé, M. Fiocchi and G. G. Malliaras, *Adv. Mater.*, 2013, **25**, 7010–7014.
21 Y. Zhang, G. Ye, T. P. A. van der Pol, J. Dong, E. R. W. van Doremaele, I. Krauhausen, Y. Liu, P. Gkoupidenis, G. Portale, J. Song, R. C. Chiechi and Y. van de Burgt, *Adv. Funct. Mater.*, 2022, **32**, 2201593.
22 J. Surgailis, A. Savva, V. Druet, B. D. Paulsen, R. Wu, A. Hamidi-Sakr, D. Ohayon, G. Nikiforidis, X. Chen, I. McCulloch, J. Rivnay and S. Inal, *Adv. Funct. Mater.*, 2021, **31**, 2010165.
23 S. Luňák, M. Weiter and M. Vala, *Chem. Phys. Chem.*, 2022, **23**, e202200252.
24 X.-X. Chen, J.-T. Li, Y.-H. Fang, X.-Y. Deng, X.-Q. Wang, G. Liu, Y. Wang, X. Gu, S.-D. Jiang and T. Lei, *Nat. Commun.*, 2022, **13**, 2258.
25 M. Ma, L. Zhang, M. Huang, Y. Kuang, H. Li, H. Yang, T. Yao, G. Ye, S. Shao, M. H. Yoon and J. Liu, *Angew. Chem., Int. Ed.*, 2025, e202424820.
26 P. Li, J. Shi, Y. Lei, Z. Huang and T. Lei, *Nat. Commun.*, 2022, **13**, 5970.
27 J. Liu, L. Qiu, R. Alessandri, X. Qiu, G. Portale, J. Dong, W. Talsma, G. Ye, A. A. Sengrian, P. C. T. Souza, M. A. Loi, R. C. Chiechi, S. J. Marrink, J. C. Hummelen and L. J. A. Koster, *Adv. Mater.*, 2018, **30**, 1704630.
28 M. Ma, L. Zhang, T. Yao, H. Yang, J. Liu and J. Liu, *Polym. Sci. Technol.*, 2025, 359–365.
29 H. Li, H. Yang, L. Zhang, S. Wang, Y. Chen, Q. Zhang, J. Zhang, H. Tian and Y. Han, *Macromolecules*, 2021, **54**, 10557–10573.
30 I. E. Jacobs, Y. Lin, Y. Huang, X. Ren, D. Simatos, C. Chen, D. Tjhe, M. Statz, L. Lai, P. A. Finn, W. G. Neal, G. D'Avino, V. Lemaur, S. Fratini, D. Beljonne, J. Strzalka, C. B. Nielsen, S. Barlow, S. R. Marder, I. McCulloch and H. Sirringhaus, *Adv. Mater.*, 2021, **34**, 2102988.
31 G. Qi, M. Wang, S. Wang, S. Zhang, X. Teng, H. Bai, B. Wang, C. Zhao, W. Su, Q. Fan and W. Ma, *Adv. Funct. Mater.*, 2024, 2413112.
32 I. Y. Jo, D. Jeong, Y. Moon, D. Lee, S. Lee, J. G. Choi, D. Nam, J. H. Kim, J. Cho, S. Cho, D. Y. Kim, H. Ahn, B. J. Kim and M. H. Yoon, *Adv. Mater.*, 2023, **36**, 2307402.
33 Y. Sun, Y. Lan, M. Li, W. Feng, M. Xie, Y. Lai, W. Li, Y. Cheng, J. Chen, W. Huang, L. W. Feng and J. Ding, *Aggregate*, 2024, **5**, e577.
34 E. Stein, O. Nahor, M. Stolov, V. Freger, I. M. Petruta, I. McCulloch and G. L. Frey, *Nat. Commun.*, 2022, **13**, 5548.
35 I. Lee, J. H. Kim, Y. Kim, D. Shin, H. Lee, J. Won, K. Kang, J. G. Choi, M. H. Yoon and S. Park, *Adv. Mater.*, 2024, **37**, 2313121.